Chinese Chemical Letters 34 (2023) 107305

Contents lists available at ScienceDirect

Chinese Chemical Letters

journal homepage: www.elsevier.com/locate/cclet

# Graphene-supported cobalt nanoparticles used to activate $SiO_2$-based anode for lithium-ion batteries

Qi An[a], Xiaohong Sun[a,*], Ying Na[a], Shu Cai[a], Chunming Zheng[b,*]

[a] School of Materials Science and Engineering, Key Laboratory of Advanced Ceramics and Machining Technology of Ministry of Education, Tianjin University, Tianjin 300072, China

[b] School of Chemistry and Chemical Engineering, State Key Laboratory of Hollow-fiber Membrane Materials and Membrane Processes, Tiangong University, Tianjin 300387, China

ARTICLE INFO

*Article history:*
Received 7 January 2022
Revised 18 February 2022
Accepted 7 March 2022
Available online 10 March 2022

*Keywords:*
Lithium-ion batteries
$SiO_2$-based anode
Graphene network
Co nanoparticles
Electrochemical activity

ABSTRACT

Although $SiO_2$-based anode is a strong competitor to supersede graphite anode for lithium-ion batteries, it still has problems such as low electrochemical activity, enormous loss of active lithium, and serious volume expansion. In order to solve these problems, we used a graphene network loaded with cobalt metal nanoparticles (rGO–Co) to coat $SiO_2$ porous hollow spheres ($SiO_2$@rGO–Co). The construction of porous hollow structure and graphene network can shorten the lithium-ion ($Li^+$) diffusion distance and enhance the conductivity of the composite, which improves the electrochemical activity of $SiO_2$ effectively. They also alleviate the volume expansion of the anode in the cycling process. Moreover, nano-scale cobalt metal particles dispersed on graphene catalyze the conversion reaction of $SiO_2$ and activate the locked $Li^+$ in $Li_2O$ through a reversible reaction, which improves the charge and discharge capacity of the anode. The capacity of $SiO_2$@rGO–Co reaches 370.4 mAh/g after 100 cycles at 0.1 A/g, which is 6.19 times the capacity of pure $SiO_2$ (59.8 mAh/g) under the same circumstance. What is more, its structure also exhibits excellent cycle stability, with a volume expansion rate of only 13.0% after 100 cycles at a current density of 0.1 A/g.



Under the vision of "Achieving Carbon Neutrality by 2050" proposed by the United Nations Climate Action Summit, many industries seek opportunities for green transformation, and the new energy storage industry is ushering in a period of rapid development. Lithium-ion batteries have received widespread consideration as a technical route with great promotion potential. However, the currently commercial graphite anodes have the disadvantages of low theoretical capacity (372 mAh/g), low lithium intercalation potential, poor rate performance and safety performance [1]. So as for improving the performance of lithium-ion batteries, researchers are looking for high theoretical capacity anode materials that can replace graphite anodes energetically. The $SiO_2$-based anode has a higher theoretical capacity than graphite anode and a smaller volume expansion rate relative to the Si-based anode [2–4], which has good commercial prospects.

However, due to the inherent poor electroconductivity of $SiO_2$ and the high bond energy of Si–O bonds, it is difficult to break Si–O bonds and activate $SiO_2$ [5,6]. Besides, the $Li_2O$ and $Li_4SiO_4$ formed by the conversion reaction are irreversible products, causing the loss of active lithium [7,8]. At the same time, $SiO_2$-based anode also has the shortcomings of slow $Li^+$ diffusion and serious volume expansion during charging and discharging [9]. These defects make $SiO_2$ very constrained in its application, and couldn't show high capacity. In brief, for its real commercialization, it is necessary to solve the problems of low electrochemical activity, enormous loss of active lithium, and serious volume expansion.

Many researchers improve the electrochemical activity of $SiO_2$ by reducing the $Li^+$ diffusion distance and enhancing the conductivity of the material. For example, preparing nano-scale $SiO_2$ [10–12], or combining it with various conductive carbon materials [13–16]. There are few studies on reducing the loss of active lithium, and some people think that compounding with conductive metal can ameliorate this situation. Shen *et al.* thermally reduced cobalt silicate to Co-$SiO_2$ composite in $Ar/H_2$, and found that cobalt particles can reduce lithium loss [17]. For the problem of serious volume expansion, many studies have made $SiO_2$ into hollow structures (*e.g.*, hollow spheres, hollow cubes, hollow nanotubes), using hollow cavities to adjust volume changes [18–21]. The hollow structure can also shorten the $Li^+$ diffusion route, create favorable conditions for improving the electrochem-

* Corresponding authors.
*E-mail addresses:* sunxh@tju.edu.cn (X. Sun), zhengchunming@tiangong.edu.cn (C. Zheng).

https://doi.org/10.1016/j.cclet.2022.03.028
1001-8417/

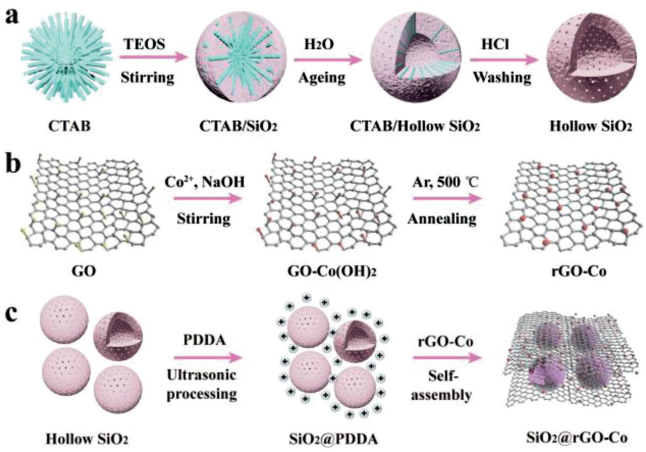


**Fig. 1.** Schematic diagram of preparing (a) $SiO_2$, (b) rGO–Co and (c) $SiO_2$@rGO–Co.

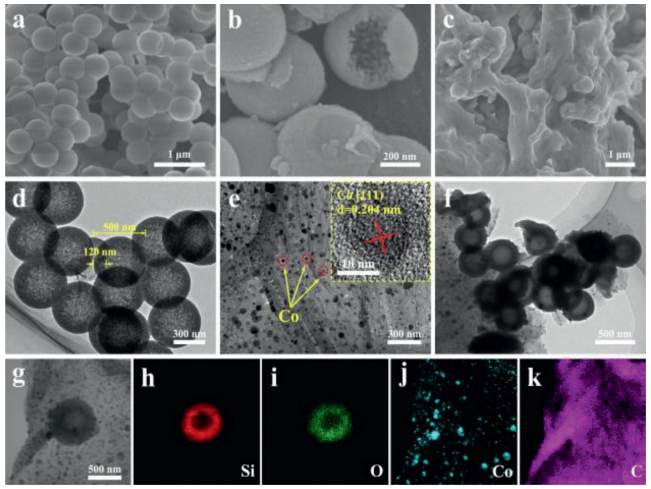


**Fig. 2.** SEM images of (a, b) pure $SiO_2$, (c) $SiO_2$@rGO composite. TEM images of (d) pure $SiO_2$, (e) rGO–Co composite, (f) $SiO_2$@rGO–Co composite. (g) TEM image and (h-k) elemental mapping results of $SiO_2$@rGO–Co composite.

ical performance of $SiO_2$. Despite the above three technical routes having been developed, there are few studies that can solve these problems at the same time, and they need further investigation.

To this end, we use graphene loaded with cobalt metal nanoparticles (rGO–Co) to coat porous hollow $SiO_2$ spheres for preparing $SiO_2$@rGO–Co composite. In the composite, graphene can improve the conductivity of the $SiO_2$ system, and can also cooperate with the porous hollow structure of silica spheres to buffer the volume expansion during cycling. More importantly, as a load matrix, it successfully introduces nano-scale Co metal particles into the system. Co nanoparticles make a significant contribution to promoting the capacity of $SiO_2$@rGO–Co. For one thing, it revamps the electrochemical activity of $SiO_2$ by catalyzing the occurrence of the $SiO_2$ conversion reaction. For another thing, it can react with the product $Li_2O$ to release $Li^+$ and reduce the loss of active lithium. Through testing, it is found that the capacity of pure $SiO_2$ after 100 cycles at 0.1 A/g is only 59.8 mAh/g, while the capacity of $SiO_2$@rGO–Co after 100 cycles reaches 370.4 mAh/g, which is 6.19 times of pure $SiO_2$. Furthermore, compared with the volume expansion rate of pure $SiO_2$ electrode after 100 cycles (112.8%), the volume expansion rate of the $SiO_2$@rGO–Co electrode is only 13.0%.

The preparation process of $SiO_2$, rGO–Co and $SiO_2$@rGO–Co is shown in Fig. 1. We synthesized pure $SiO_2$ with the surfactant-assisted sol-gel method reported in the literature [22]. As shown in Fig. 1a, the $SiO_2$ molecules produced by the hydrolysis of tetraethyl orthosilicate (TEOS) are electrostatically adsorbed to the surface of the cetyl-methyl-ammoniumbromide (CTAB) surfactant to form mesoporous silica spheres. Then, it is aged in a deionized water solution. During the aging process, water molecules diffuse through the mesopores into the CTAB/$SiO_2$ composite frame quickly. There are plentiful Si–$OC_2H_5$ groups with a low degree of cross-linking in the core of the silica spheres. Compared with the shell, it is more likely to be corroded and dissolved by water [22]. With the passage of aging time, the inside of the mesoporous silica spheres is continuously etched, and finally transformed into porous hollow spheres. Fig. 1b illustrates the process of preparing rGO–Co composites by thermal reduction [23]. The functional groups (*e.g.*, hydroxyl, carboxyl) on the graphene surface would attract $Co^{2+}$ to anchor it on the graphene electrostatically. After adding NaOH solution, $Co^{2+}$ would constitute $Co(OH)_2$ and precipitate upon the graphene. In the subsequent calcination process, the CO gas released by graphene can reduce $Co(OH)_2$ to Co nanoparticles *in situ*, thus synthesizing rGO–Co composites successfully. $SiO_2$@rGO–Co was self-assembled by electrostatic action to form an encapsulation structure. As displayed in Fig. 1c, we first treat $SiO_2$ porous hollow spheres with poly dimethyl diallyl ammonium chloride (PDDA) to obtain positively charged $SiO_2$@PDDA on the surface, and then mix it with the negatively charged rGO–Co fully. They react electrostatically and form $SiO_2$@rGO–Co composite materials spontaneously. We replaced rGO–Co with rGO, prepared $SiO_2$@rGO, and used it as a comparative sample to analyze the effect of Co nanoparticles.

We adopted SEM and TEM to study the micromorphology of pure $SiO_2$, $SiO_2$@rGO, and $SiO_2$@rGO–Co samples. As depicted in Fig. 2a, the pure $SiO_2$ synthesized by the template-free method is spheres of uniform size and a mean diameter of nearly 500 nm. Figs. 2b and d reveal the hollow structure of the sphere clearly, and its average wall thickness is approximately 120 nm. The surface of the inner wall for the hollow sphere is rough, indicating that the formation of cavities has undergone the transformation of the internal structure. This is confirmed by the hollow structure formation mechanism as previously mentioned. Fig. 2c gives a SEM image of $SiO_2$@rGO. It can be seen that the graphene sheets are soft and continuous, and the spherical protrusions on the surface demonstrate that the hollow $SiO_2$ spheres are successfully wrapped in the graphene frame. Fig. 2e displays the size and dispersion of the Co metal particles in the rGO–Co composite. Co metal is mostly nanoparticles between 10 nm and 30 nm and dispersed inside or upon the graphene network evenly. From the HR-TEM image (inset of Fig. 2e), we can find the lattice spacing is 0.204 nm, which matches the (111) crystal plane of the cubic phase Co. The TEM image of the $SiO_2$@rGO–Co sample (Fig. 2f) presents that the hollow $SiO_2$ is covered by rGO–Co. The uniformity of $SiO_2$@rGO–Co can be observed from the SEM (Figs. S1a and b in Supporting information) and TEM images (Figs. S1c-f in Supporting information). As shown in figures, most of the $SiO_2$ spheres are coated inside the soft rGO–Co sheets, and a small number of $SiO_2$ spheres are scattered on the surface of rGO–Co. There is no massive agglomeration of $SiO_2$ or rGO–Co, and the overall distribution of the material is relatively uniform. Its TEM images and element mapping results are delineated in Figs. 2g-k. The elemental distribution of Si and O proves the hollow structure of $SiO_2$, and the elemental distribution of Co and C shows the dispersion of Co nanoparticles on graphene. The elemental mapping results can also further illustrate that rGO–Co has achieved the coating to hollow $SiO_2$.

It is known from the preparation mechanism of pure $SiO_2$ that hollow spheres contain mesopores. For this reason, we analyzed the specific surface area and pore structure of the prepared sam-

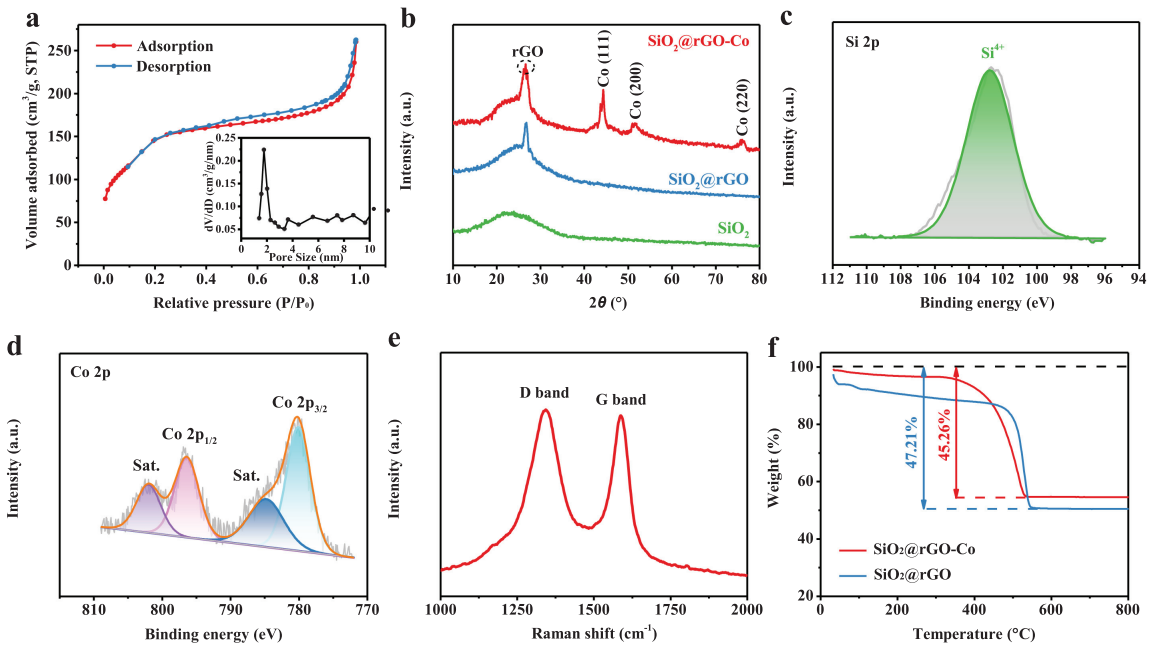


**Fig. 3.** (a) Nitrogen absorption and desorption curve and pore size distribution of $SiO_2$@rGO–Co. (b) XRD patterns of the pure $SiO_2$, $SiO_2$@rGO and $SiO_2$@rGO–Co. High resolution XPS spectra of (c) Si 2p and (d) Co 2p for $SiO_2$@rGO–Co. (e) Raman spectrum of $SiO_2$@rGO–Co. (f) TG curves of $SiO_2$@rGO and $SiO_2$@rGO–Co.

ples through the nitrogen adsorption and desorption curve and the pore size distribution curve. Fig. S2 (Supporting information) shows the test results of pure $SiO_2$ hollow spheres. The curve is IV type isotherm and with H4 type hysteresis loop, which is a typical mesoporous structure material [24]. The specific surface area of the pure $SiO_2$ hollow sphere measured by the BET method is 773.5 $m^2/g$. Based on the BJH method to calculate the pore size distribution, it is found that the hollow sphere has uniform mesopores of 2 nm. These mesopores provides a channel for the diffusion of water molecules into the spherical shell during the formation of the $SiO_2$ porous hollow structure. What is more, the rate of in and out of $Li^+$ during the charge/discharge cycle can be increased [25]. Fig. 3a exhibits the $N_2$ adsorption and desorption curve and the pore size distribution curve of $SiO_2$@rGO–Co. Compared with $SiO_2$, the type of isotherm has not changed, and the material still has a mesoporous structure and the pore size distribution is about 2 nm. The specific surface area calculated by BET is 388.2 $m^2/g$, which is lower than pure $SiO_2$. The decrease of the specific surface area is due to the mesoporous channels in the porous hollow spheres being covered by the cobalt-loaded graphene sheets [26]. This is also in keeping with the results detected through the TEM image (Fig. 2f).

After characterizing the structure of samples, we explored the phase composition of the three samples. Fig. 3b compares the X-ray diffraction results of $SiO_2$, $SiO_2$@rGO and $SiO_2$@rGO–Co. As shown in the figure, they all have an obvious roomy peak around 22°, indicating the existence of amorphous $SiO_2$ [27]. $SiO_2$@rGO and $SiO_2$@rGO–Co both show a diffraction peak matched to the (002) crystal plane of graphene at about 26° [28]. In addition, there are three diffraction peaks at 44.3°, 51.3° and 76.1° in the XRD pattern of $SiO_2$@rGO–Co. It has been verified that they are corresponding to the (111), (200) and (220) crystal planes of the Co face-centered cubic structure (JCPDS 15–0806, FCC phase). The diffraction peaks are broad, illustrating that the Co particles are nano-sized [29]. The XRD pattern again proves the existence of Co nanoparticles, and no other obvious impurity peaks are found. Besides, we used XPS to further characterize the valence states of each element in $SiO_2$@rGO–Co. As shown in Fig. 3c, a characteristic peak of Si $2p_{3/2}$ is observed at 102.8 eV, demonstrating that the Si is in the form of $Si^{4+}$ [30]. The Co 2p high-resolution spectrum is displayed in Fig. 3d. There are two characteristic peaks with a weak intensity that appeared at 780.1 eV and 796.5 eV, corresponding to the $2p_{3/2}$ and $2p_{1/2}$ peaks of $Co^{2+}$, respectively [31–33]. The partial oxidation of the surface for Co particles exposed to the air environment cause the presence of $Co^{2+}$ in the sample. However, the XRD spectrum of $SiO_2$@rGO–Co shows Co is a simple substance. Therefore, most Co nanoparticles are still in the form of crystalline metal. Raman spectroscopy was performed on the $SiO_2$@rGO–Co (Fig. 3e) to analyze the degree of disorder for graphene. The D peak at 1350 $cm^{-1}$ and the G peak at 1586 $cm^{-1}$ were observed in Raman spectroscopy. Compared with the G peak, the intensity of D peak is greater, which manifests that the rGO becomes more disordered after loading the Co nanoparticles, and the conductivity is better [12,34]. This is also consistent with the phenomenon that graphene in the XRD spectrum shows a bun peak with a high background signal intensity. Next, we conducted an ICP-AES test to analyze the content of each component quantitatively in the $SiO_2$@rGO–Co sample. We list the element mass fractions of Si and Co in Table S1 (Supporting information). According to the data in the table, the content of $SiO_2$, rGO, and Co in the sample is calculated to be 41.72 wt%, 51.29 wt%, and 6.99 wt%, respectively. Furthermore, we carried out thermogravimetric tests on $SiO_2$@rGO and $SiO_2$@rGO–Co in the air to determine the rGO content in the system. The blue curve in Fig. 3f represents the test result of $SiO_2$@rGO, in which the content of rGO is 47.21 wt% and the content of $SiO_2$ is 52.79 wt%. The $SiO_2$@rGO–Co represented by the red curve has a mass loss of 45.26 wt%. It is slightly different from the rGO content calculated through the ICP test results. This is because the final product of $SiO_2$@rGO–Co after the thermogravimetric test is $SiO_2/Co_3O_4$. The weight gain of the oxidation for the Co element offsets the weight loss of carbon decomposition, so that the weight loss reflected by the sample is less than its actual carbon content. We can also observe that the initial weight loss of $SiO_2$@rGO–Co is slower than that of $SiO_2$@rGO obviously

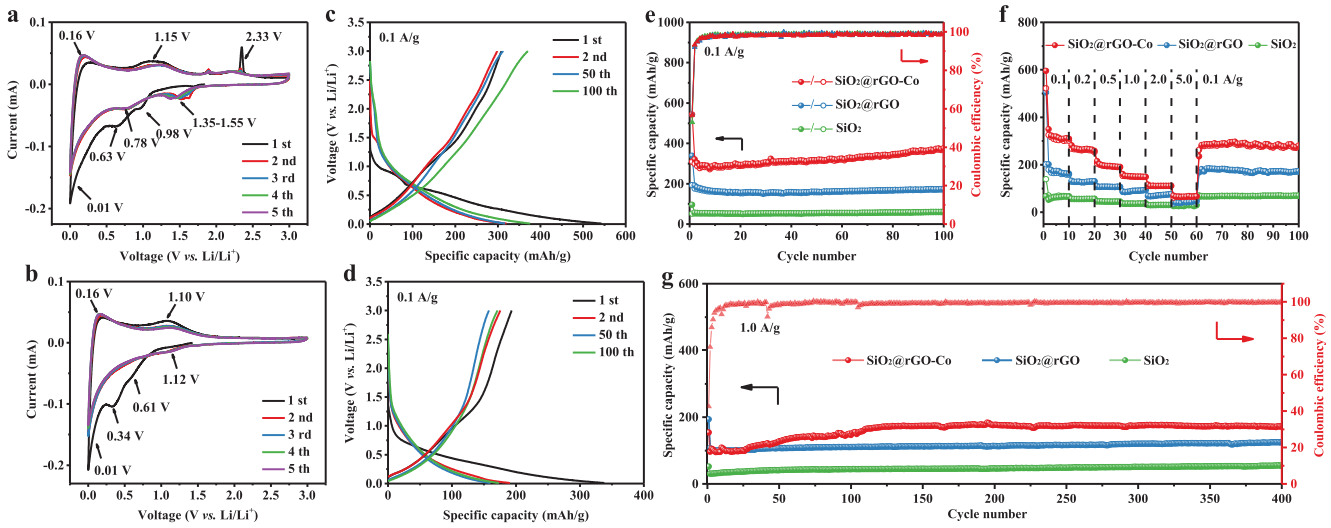


**Fig. 4.** (a) CV curves of $SiO_2$@rGO–Co. (b) CV curves of $SiO_2$@rGO. (c) Charge/discharge curves of $SiO_2$@rGO–Co. (d) Charge/discharge curves of $SiO_2$@rGO. (e) Cycling performance of $SiO_2$@rGO–Co, $SiO_2$@rGO and pure $SiO_2$ at 0.1 A/g. (f) Rate performance of $SiO_2$@rGO–Co, $SiO_2$@rGO and pure $SiO_2$. (g) Cycling performance of $SiO_2$@rGO–Co, $SiO_2$@rGO and pure $SiO_2$ at 1.0 A/g.

from Fig. 3f. This phenomenon also corresponds to the quality compensation effect of the formation of $Co_3O_4$ on the system.

With $SiO_2$@rGO–Co as the positive electrode and lithium metal as the negative electrode, a half-cell was assembled to analyze the electrochemical behavior of the material. Fig. 4a displays the first five CV curves of $SiO_2$@rGO–Co under the voltage window of 0.01–3.0 V (*vs.* $Li^+$/Li). The reduction peak at ~0.98 V in the first scan can be attributable to the conversion reaction between $SiO_2$ and Si (Eqs. 1–3) [35]. Among them, only the reaction in Eq. 2 is reversible, and the other two reactions in which the product is $Li_2O$ (Eq. 1) and $Li_4SiO_4$ (Eq. 3) are both irreversible. Their irreversibility will cause a large amount of active lithium loss, result in a poor charge/discharge capacity of $SiO_2$. The broad peak at ~0.63 V is because of the decomposition of the electrolyte and the formation of the solid electrolyte interface (SEI) film during the first cycle of discharge [2], and it disappears in consequent cycles. The reduction peak at ~0.01 V corresponds to the alloying reaction of Si and Li (Eq. 4), while the oxidation peak at ~0.16 V is the result of the $Li_xSi$ dealloying reaction during the charging process (Eq. 4). The lithium storage capacity is contributed by this pair of redox reactions mainly. Next, an oxidation peak arise at around 1.15 V, which might be due to the reversible conversion reaction between $Li_2Si_2O_5$ and $SiO_2$ (Eq. 2) [36]. The corresponding reduction peak moved from ~0.98 V in the first lap to ~0.78 V in the next few cycles. The increase of the potential difference between oxidation and reduction peak indicates that the invertibility of the conversion reaction has decreased slightly, which is related to the irreversibility of Eqs. 1 and 3. Significantly, an oxidation peak is observed at ~2.33 V. It is verified that this peak corresponds to the oxidation reaction of Co and $Li_2O$ (Eq. 5) [17,37]. $Li_2O$ is the product of the irreversible conversion reaction of $SiO_2$ (Eq. 1). During this process, Co nanoparticles react with $Li_2O$, thereby releasing a mass of $Li^+$ to reactivate it in subsequent cycles, avoiding an enormous loss of active lithium. In the next cycle, the formed CoO is reduced to Co through the lithiation reaction (Eq. 5), which can be confirmed by observing the reduction peak at ~1.35–1.55 V [17,37]. The reversibility of this reaction proves that Co nanoparticles can repeatedly activate $Li_2O$. The potential of the reduction peak gradually decreases from 1.55 V to 1.35 V with cycling, which may be related to electrode polarization. This is very common, and the same phenomenon has manifested in other works [38–40]. Specifically, the activation polarization caused by the retardation of the charge transfer process in the electrode-electrolyte interface layer, and the concentration polarization caused by the retardation of the mass transfer process in the electrode-electrolyte interface layer, resulting in a negative shift of the reduction peak potential. But it is worth noting that the reduction peaks basically coincided with the fourth and fifth circles, indicating that the electrode has reached a stable state and will not further affect the later cycle process. On the whole, except for the first cycle of charge/discharge curve, the other CV curves almost overlap, presenting that $SiO_2$@rGO–Co has a highly reversible process of (de)intercalating lithium. The specific electrochemical reaction equations are listed as follows [30]:

$$SiO_2 + 4Li^+ + 4e^- \rightarrow 2Li_2O + Si \quad (1)$$

$$5SiO_2 + 4Li^+ + 4e^- \leftrightarrow 2Li_2Si_2O_5 + Si \quad (2)$$

$$2SiO_2 + 4Li^+ + 4e^- \rightarrow Li_4SiO_4 + Si \quad (3)$$

$$Si + xLi^+ + xe^- \leftrightarrow Li_xSi \quad (4)$$

$$CoO + 2Li^+ + 2e^- \leftrightarrow Co + Li_2O \quad (5)$$

For the sake of investigating the difference in electrochemical behavior between $SiO_2$@rGO–Co and the contrast sample, we ran a CV test on $SiO_2$@rGO under the same conditions (Fig. 4b). The reactions of the two samples are roughly the same. In the first circle of scanning, the formation of SEI film caused the broad peaks at ~0.61 V and ~0.34 V [41], and they disappear in the next cycles. An extremely inconspicuous broad peak is noticed at ~1.12 V, which may correspond to the conversion reaction of $SiO_2$ (Eqs. 1-3). There are two pairs of redox peaks in next cycles. The first pair of peaks (0.16 V/~0.01 V) corresponds to the (de)alloying reaction between Si and $Li_xSi$ (Eq. 4). The second pair of peaks (1.10 V/1.12 V) is the reversible redox reaction peak between $SiO_2$ and $Li_2Si_2O_5$ (Eq. 2). Differently, there is no redox peak at 2.33 V/1.35–1.55 V. It further proves that this pair of peaks in $SiO_2$@rGO–Co belong exclusively to the reversible reaction between Co and CoO. Comparing the two sets of CV curves carefully, it can be found that the intensity of the reduction peak (~1.12 V) in Fig. 4b is significantly lower than the intensity of the reduction peak (~0.98 V and ~0.78 V) in Fig. 4a. This reduction peak represents the conversion reaction from $SiO_2$ to Si. It shows that the conversion reaction of

$SiO_2$@rGO–Co is more intense than that of $SiO_2$@rGO. This may be because Co nanoparticles are helpful to break the Si–O bonds [42], catalyze the occurrence of the $SiO_2$ conversion reaction, and improve the electrochemical activity of $SiO_2$.

Figs. 4c and d are the charge/discharge curves of $SiO_2$@rGO–Co and $SiO_2$@rGO at different cycles under 0.1 A/g current density, respectively. The voltage of the ramp platform in the charge/discharge curves of them is in accordance with the peak position in the corresponding CV curves. In addition, the first-lap discharge capacity of $SiO_2$@rGO–Co can reach 543.2 mAh/g, and the charge capacity is 310.2 mAh/g (Fig. 4c). In comparison, the first-lap discharge capacity and charge capacity of $SiO_2$@rGO are only 338.3 mAh/g and 192.2 mAh/g (Fig. 4d). The huge difference in initial capacity between $SiO_2$@rGO–Co and $SiO_2$@rGO is precisely due to the different degree of their conversion reactions. This corresponds to the phenomenon that the intensity of the reduction peak in the CV curve is different. It is attested that the existence of Co particles is beneficial to the $SiO_2$ conversion reaction. The initial coulombic efficiencies (ICE) of $SiO_2$@rGO–Co and $SiO_2$@rGO are 57.1% and 56.8%. The reason for the low ICE is that SEI film is generated during the first lithium insertion process and a large number of irreversible products are produced. This problem is common in $SiO_2$-based anode materials [20,25,43].

Fig. 4e provides the cycle performances of $SiO_2$, $SiO_2$@rGO, and $SiO_2$@rGO–Co at a current density of 0.1 A/g. Owing to its poor conductivity and low electrochemical activity, pure $SiO_2$ only contributed a capacity of 95.8 mAh/g amid the first cycle of discharge. Since the serious loss of active lithium during the charging process, only a charge capacity of 50.8 mAh/g was obtained. After 100 cycles, the discharge capacity remained at 59.8 mAh/g. The first lap charge capacity of $SiO_2$@rGO was 192.2 mAh/g, and it stabilized at 171.3 mAh/g after 100 cycles. With the help of the graphene conductive network, the capacity of $SiO_2$@rGO was increased compared with pure $SiO_2$. The electrons in the $SiO_2$@rGO sample had the opportunity to reach the surface of more $SiO_2$ particles and can achieve rapid migration, thereby obtaining higher electrochemical activity. $SiO_2$@rGO–Co had the most outstanding electrochemical performance among the three samples. Its first lap charge capacity was as high as 310.2 mAh/g, and after 100 cycles, it climbed to 370.4 mAh/g. The further increase in the capacity of $SiO_2$@rGO–Co benefits from the catalysis of Co nanoparticles on the conversion reaction and the activation of dead lithium. The phenomenon of capacity climb is very common in metal oxide anodes [44–46]. We suspect that there may be two reasons for $SiO_2$@rGO–Co anode. First, the electrode was activated and the quantity of active sites for lithium storage increased as the cycle progresses. And the charge transfer resistance ($R_{ct}$) was reduced so that the capacity was improved continuously [46]. Second, the repeated activation of Co nanoparticles to $Li_2O$ made the concentration of $Li^+$ in the electrolyte enhance gradually. As the amount of $Li^+$ that can be stored rase, the capacity improved accordingly. The rate performance of $SiO_2$@rGO–Co also has advantages that the other two samples cannot match (Fig. 4f). At current densities of 0.1, 0.2, 0.5, 1.0, 2.0 and 5.0 A/g, the average discharge capacity is 310.4, 270.1, 198.2, 154.8, 112.7 and 70.4 mAh/g. When the current density is restored to 0.1 A/g, the discharge capacity can be recovered to 306.6 mAh/g, which is slightly lower than 310.4 mAh/g in the initial state. Similar phenomenon has emerged in the work of others [47–49]. This is due to the failure of some active materials under the impact of the mechanical effect (crack propagation and particle breakage that occur on different scales) of a large current, resulting in a loss of capacity and a decrease in performance. Long cycle performance is an important quality to measure the pros and cons of electrode material. For this reason, we tested the cycle stability of three samples under a large current of 1.0 A/g. As shown in Fig. 4g, the discharge capacity of $SiO_2$@rGO–Co reached 171.3 mAh/g after 400 cycles at 1.0 A/g, which was higher than the 124.5 mAh/g and 54.8 mAh/g of $SiO_2$@rGO and pure $SiO_2$. Fig. S3 (Supporting information) demonstrates the discharge capacity of $SiO_2$@rGO–Co for 2000 cycles at a current density of 1.0 A/g. Its initial discharge capacity is 154.1 mAh/g, and after 2000 cycles, it still retains 144.9 mAh/g, and the capacity retention rate is 94.03%. The above test results show that the catalysis and activation of Co nanoparticles and the construction of the graphene conductive network form a synergistic effect, which is crucial to the excellent performance of $SiO_2$@rGO–Co.

We performed electrochemical AC impedance tests on three samples to explore the effects of Co nanoparticles and rGO on the charge transfer characteristics and the $Li^+$ diffusion coefficient of $SiO_2$. The frequency range of the given disturbance signal is 0.1 Hz-100 kHz, and the test results are plotted in the form of a Nyquist diagram (Fig. S4a in Supporting information). The inset shows the equivalent circuit used. It can be seen from the figure that their Nyquist diagrams were composed of a semicircle in the high-frequency region and a straight line with an inclination angle close to 45° in the low-frequency region. This shows that the electrode process is controlled by a mixture of charge transfer and diffusion processes. From the semicircle in Fig. S4a, the fitted values of ohmic resistance ($R_s$) and charge transfer resistance ($R_{ct}$) can be read, as listed in Table S2 (Supporting information). The $R_s$ of pure $SiO_2$, $SiO_2$@rGO and $SiO_2$@rGO–Co are all around 3 Ω, while $R_{ct}$ is 215.80 Ω, 129.63 Ω and 98.04 Ω, respectively. It shows that the conductivity of Co nanoparticles and graphene network can improve the charge transfer ability of the system. The diffusion process of the electrode will cause the concentration polarization to produce the Warburg impedance, so the evaluation of the $Li^+$ diffusion coefficient can be realized by calculating Warburg coefficients. The specific formula used is listed in (Eqs. S1 and S2 (Supporting information) [1]. According to Eq. S2, we drew a scatter plot with $Z'$ as the ordinate and $\omega^{-1/2}$ as the abscissa (Fig. S4b in Supporting information), fitted it to a straight line and got the slope. The slope value represents the $\sigma$ of different samples. Then substituting the constants into Eq. S1 to calculate the $Li^+$ diffusion coefficients of different samples. The $Li^+$ diffusion coefficients of pure $SiO_2$, $SiO_2$@rGO and $SiO_2$@rGO–Co were $7.712 \times 10^{-15}$, $1.527 \times 10^{-14}$ and $1.544 \times 10^{-14}$ $cm^2/s$, severally. The calculation results illustrate that the diffusion coefficients of the graphene-containing samples are increased by an order of magnitude compared with that of pure $SiO_2$. This may be due to the fact that the nanometer scale of graphene sheets greatly shortens the $Li^+$ diffusion path, and the sheet spacing is also conducive to the diffusion and transport of $Li^+$. Compared with $SiO_2$@rGO, $SiO_2$@rGO–Co has a slight increase in diffusion coefficient but little change, indicating that Co nanoparticles are not the main reason for the advance in lithium ion diffusion coefficient. In addition, we also tested the impedance of $SiO_2$@rGO–Co after 1 cycle, 50 cycles and 100 cycles at 0.1 A/g. As shown in Figs. S4c and d (Supporting information), $R_{ct}$ is 98.04 Ω, 87.87 Ω and 60.79 Ω, respectively, showing a decreasing trend. This confirms our conjecture that the increasing capacity of $SiO_2$@rGO–Co is due to the decreasing $R_{ct}$.

In the process of charging and discharging, the volume expands sharply and the electrode pulverization is severe, which has always been one of the urgent problems to be solved for the $SiO_2$-based anodes. Therefore, we took SEM images of the electrode before and after 100 cycles at a current density of 0.1 A/g to explore the volume change before and after cycling of the sample and the pulverization of the electrode. Figs. S5a and b (Supporting information) are the cross-sectional views of the pure $SiO_2$ electrode sheet before and after cycling. It can be observed that its thickness changes from 14.1 μm to 30.0 μm, and the volume expansion rate reaches 112.8%. And there is a crack across the entire cross section, which indicates that the electrode sheet has a serious volume expansion

during the cycle and the active material has a tendency to peel off from the current collector. However, the volume expansion rate of ordinary silica materials is close to 290% [50]. Compared with them, $SiO_2$ porous hollow spheres have obvious advantages, which proves that the porous hollow structure of $SiO_2$ can absorb part of the huge strain caused by volume expansion. Figs. S5c and d (Supporting information) are the SEM images of $SiO_2$@rGO electrode before and after 100 cycles. The volume expansion rate calculated from the thickness data in the figure is 19.2%. The sharp decrease in the expansion rate than pure $SiO_2$ indicates that the flexible coating of graphene buffers the volume expansion of the electrode. The volume expansion rate of the $SiO_2$@rGO–Co electrode (Figs. S5e and f in Supporting information) is only 13.0%. A possible explanation may be, the Co nanoparticles take advantage of their ductility and mechanical strength to further alleviate the damage to the electrode structure caused by volume changes [51]. To fully understand the ability of $SiO_2$@rGO–Co to buffer volume expansion, we explored the volume expansion rate of the electrode after 1000 cycles at higher current density (1.0, 2.0 and 5.0 A/g). As shown in Figs. S6a-c (Supporting information), the thicknesses of the electrode sheets after cycling are 24.1 μm, 27.2 μm and 28.5 μm, respectively, and the corresponding volume expansion ratios are 30.98%, 47.83% and 54.89%. The test results show that the mechanical effect brought by the high current impact has a negative impact on the structure of the pole piece. As the current density increases, the volume expansion rate continues to increase. This phenomenon is confirmed by the rate performance test results. However, under the high current of 5.0A/g, the volume expansion rate is only 54.89%, and the material shows obvious advantages in buffering volume expansion. Figs. S7a and d (Supporting information) are the surface conditions of the pure $SiO_2$ electrode sheet before and after cycling. It can be observed that a huge and deep crack with a diameter of about 2 μm appears on the surface of electrode sheet, indicating that the electrode has a serious chalking phenomenon. After the cycles of $SiO_2$@rGO (Figs. S7b and e in Supporting information) and $SiO_2$@rGO–Co (Figs. S7c and f in Supporting information), there are almost no cracks or only tiny cracks on the surface. It further illustrates the important role of graphene and Co nanoparticles in inhibiting $SiO_2$ body expansion and electrode pulverization.

The previous series of performance tests proved that $SiO_2$@rGO–Co has the most excellent electrochemical performance and potential application value as an anode for lithium-ion batteries compared to $SiO_2$@rGO and $SiO_2$. We analyzed deeply and summarized the reasons for its good performance, mainly in the following aspects.

First, the porous hollow structure of the silica spheres is conducive to increase the rate of $Li^+$ in and out during the cycle, which can improve the charge and discharge performance of the sample to a certain extent. The comparison of the morphological structure (Fig. S8 in Supporting information) and electrochemical performance (Fig. S9 in Supporting information) of solid $SiO_2$ and porous hollow $SiO_2$ given in the supporting information can proof this conjecture.

Second, Co nanoparticles play a vital role in improving the charge and discharge capacity of electrode materials. On the one hand, it can catalyze the conversion reaction. As shown in Fig. 5a, $SiO_2$ must first be converted into Si through the conversion reaction, and then the alloying reaction of the Si element can be used to achieve lithium storage. Under normal circumstances, the electrochemical activity of $SiO_2$ is small, and the conversion reaction is difficult to occur [52]. However, the conductivity and catalysis of Co nanoparticles make it easy to change from $Si^{4+}$ to $Si^0$, which contribute to improve the lithium storage capacity. On the other hand, as shown in Fig. 5b, the Co nanoparticles can also undergo a reversible redox reaction with the irreversible product $Li_2O$ of the conversion reaction. The dead lithium is repeatedly activated

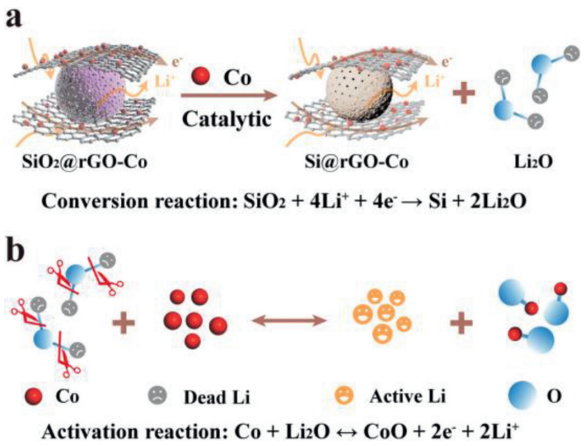


**Fig. 5.** (a) Schematic diagram of Co-catalyzed $SiO_2$ conversion reaction. (b) Mechanism diagram of Co particles activating $Li_2O$.

to reduce the loss of active lithium and increase the capacity of the sample. In order to prove that the oxidation reaction of Co nanoparticles at 2.33 V ($Co + Li_2O \rightarrow CoO + 2e^- + 2Li^+$) does have an essential activation effect. We tested the cycling performance of $SiO_2$@rGO–Co and $SiO_2$@rGO at a current density of 0.1 A/g by controlling the electrochemical window at 0.01–1.5 V. As demonstrated in Fig. S10 (Supporting information), when tested in the voltage range of 0.01–1.5 V, the capacities of $SiO_2$@rGO–Co and $SiO_2$@rGO after 100 cycles are 145.9 mAh/g and 144.2 mAh/g, respectively. Their capacity is almost the same, and the Co-containing samples did not display a significant advantage. Both are much lower than the capacity of $SiO_2$@rGO–Co at 0.01–3.0 V. This phenomenon strongly proves that the oxidation reaction of Co nanoparticles at 2.33 V can activate $Li_2O$ and reduce the loss of active lithium to improve the electrochemical performance of $SiO_2$@rGO–Co.

Third, the graphene network also played a fundamental role in promoting capacity. It can advance the conductivity of the material and the charge transfer ability in the redox process, shorten the $Li^+$ diffusion path, and increase the $Li^+$ diffusion coefficient. At the same time, as the supporting matrix of Co particles, since the arrangement of the hydroxyl groups, carboxyl groups and other groups on the graphene is relatively dispersed, the $Co^{2+}$ electrostatically adsorbed by them can also maintain dispersibilityand avoid agglomeration [23]. Maintaining its nano-scale provides a prerequisite for the activation of $Li_2O$. This could be elucidated by the lithium storage mechanism of the transition metal oxide CoO. Unlike the classical intercalation reaction mechanism of graphite, CoO has good crystallinity and cannot provide empty lithium storage sites. Unlike metals such as Si, which can form alloys with Li, in fact, it realizes lithium storage through a reversible redox reaction. The reaction equations are shown in Eqs. 6 and 7 [53]:

$$\text{Lithiation: } CoO + 2Li \rightarrow Co + Li_2O \quad (6)$$

$$\text{Delithiation: } Co + Li_2O \rightarrow CoO + 2Li \quad (7)$$

Since $Li_2O$ has stronger thermodynamic stability than CoO, the reaction of Eq. 6 can occur spontaneously, while the reaction of Eq. 7 requires some additional conditions. Studies have indicated that when the size of Co metal particles is reduced to the nanometer scale, it can effectively activate the electrochemically inert $Li_2O$, break the Li-O bond, and promote the occurrence of the reaction (Eq. 7) [53]. Therefore, the nano-Co element supported on the surface of graphene can realize the reaction of Eq. 7 smoothly, provide a guarantee for activation of $Li_2O$, and increase the charge/discharge capacity of the system.

Finally, the porous hollow structure of the silica sphere, the flexible coating of graphene and the mechanical strength of the Co particles have a synergistic effect that can effectively inhibit the volume expansion and electrode powdering during the $SiO_2$ lithium storage process, greatly improving the cycle stability of the sample.

In summary, we adopted the electrostatic self-assembly method to realize the coating of porous hollow silica spheres by the graphene loaded with Co nanoparticles. The unique porous hollow sphere structure and graphene conductive network can shorten the diffusion path of $Li^+$, improve the electrochemical activity of $SiO_2$, and buffer the drastic volume changes during the charge/discharge of the anode at the same time. Graphene can be used as the supporting matrix to maintain the nano-scale of the Co element effectively. Co nanoparticles can achieve the catalysis of the $SiO_2$ conversion reaction and the activation of the irreversible product $Li_2O$ successfully, which reducing the loss of active lithium and improving the charge and discharge performance of the material. The results indicated that the capacity of $SiO_2$@rGO–Co composite reached 370.4 mAh/g after 100 cycles at 0.1 A/g, which increased the capacity by ~500% compared to 59.8 mAh/g of pure $SiO_2$. This work provides a new idea for the strategy of using transition metals to enhance the electrochemical activity of $SiO_2$. $SiO_2$@rGO–Co composite is a kind of anode material of lithium-ion batteries with potential application value.

## Declaration of competing interest

We declared that we have no conflicts of interest to this work.

## Acknowledgments

This work was supported by the National Natural Science Foundation of China (NSFC, Nos. 52073212, 51772205, 51772208), and the General Program of Municipal Natural Science Foundation of Tianjin (Nos. 17JCYBJC17000, 17JCYBJC22700).

## References

[1] N. Zhou, Y. Wu, Y. Li, et al., Appl. Surf. Sci. 500 (2020) 144026.
[2] S. Kuang, D. Xu, W. Chen, et al., Appl. Surf. Sci. 521 (2020) 146497.
[3] D. Jia, K. Wang, J. Huang, Chem. Eng. J. 317 (2017) 673–686.
[4] Z. Sun, F. Xin, C. Cao, et al., Nanoscale 7 (2015) 20426–20434.
[5] S.P. Beltran, G.E.R. Caballero, P.B. Balbuena, J. Phys. Chem. C 119 (2015) 16424–16431.
[6] Z. Liu, Q. Yu, Y. Zhao, et al., Chem. Soc. Rev. 48 (2019) 285–309.
[7] Y. Nagao, H. Sakaguchi, H. Honda, et al., J. Electrochem. Soc. 151 (2004) A1572–A1575.
[8] T. Chen, J. Wu, Q. Zhang, et al., J. Power Sources 363 (2017) 126–144.
[9] Y. Zhang, Y. Li, Z. Wang, et al., Nano Lett. 14 (2014) 7161–7170.
[10] Y. Sun, N. Liu, Y. Cui, Nat. Energy 1 (2016) 1–12.
[11] B. Guo, J. Shu, Z. Wang, et al., Electrochem. Commun. 10 (2008) 1876–1878.
[12] X. Guo, K. Xie, Y. Wang, et al., Int. J. Electrochem. Sci. 13 (2018) 5645–5653.
[13] L. Zhang, Int. J. Electrochem. Sci. 11 (2017) 10221–10229.
[14] Q. Tian, Y. Chen, F. Chen, et al., J. Alloy. Compd. 809 (2019) 151793.
[15] H. Wang, P. Wu, M. Qu, et al., ChemElectroChem 2 (2015) 508–511.
[16] Y. Liu, N. Zhang, L. Jiao, et al., Adv. Mater. 27 (2015) 6702–6707.
[17] Y. Shen, Z. Cao, Y. Wu, et al., J. Mater. Chem. A 8 (2020) 12306–12313.
[18] X. Liu, Y. Chen, H. Liu, et al., J. Mater. Sci. Technol. 33 (2017) 239–245.
[19] H. Wang, P. Wu, H. Shi, et al., J. Power Sources 274 (2015) 951–956.
[20] X. Ma, Z. Wei, H. Han, et al., Chem. Eng. J. 323 (2017) 252–259.
[21] N. Zhang, Y. Wang, M. Jia, et al., Chem. Commun. 54 (2018) 1205–1208.
[22] Z. Teng, X. Su, Y. Zheng, et al., Chem. Mater. 25 (2013) 98–105.
[23] X. Huang, G. Zhao, X. Wang, RSC Adv. 5 (2015) 49973–49978.
[24] G. Wang, Z. Wen, Y. Yang, et al., J. Mater. Chem. A 6 (2018) 7557–7565.
[25] N. Yan, F. Wang, H. Zhong, et al., Sci. Rep. 3 (2013) 1–6.
[26] W. An, J. Fu, J. Su, et al., J. Power Sources 345 (2017) 227–236.
[27] X. Xu, H. Zhang, Y. Chen, et al., J. Alloy. Compd. 677 (2016) 237–244.
[28] H. Liu, J. Huang, X. Li, et al., Appl. Surf. Sci. 258 (2012) 4917–4921.
[29] B. Wan, J. Guo, W. Lai, et al., J. Alloy. Compd. 843 (2020) 156050.
[30] M. Zhu, Y. Shen, L. Chang, et al., Nanoscale 12 (2020) 13442–13449.
[31] Q. Dong, Y. Zhang, Z. Dai, et al., Nano Res. 11 (2018) 1389–1398.
[32] B. Li, P. Gu, Y. Feng, et al., Adv. Funct. Mater. 27 (2017) 1–11.
[33] Q. Dong, J. Yang, M. Wu, et al., Acs Sustain. Chem. Eng. 6 (2018) 15591–15597.
[34] M. Srivastava, M.Elias Uddin, J. Singh, et al., J. Alloy. Compd. 590 (2014) 266–276.
[35] L. Zhang, X. Gu, C. Yan, et al., Acs Appl. Mater. Inter. 10 (2018) 44463–44471.
[36] J. Tu, Y. Yuan, P. Zhan, et al., J. Phys. Chem. C 118 (2014) 7357–7362.
[37] F. Mueller, D. Bresser, N. Minderjahn, et al., Dalton Trans. 43 (2014) 15013–15021.
[38] L. Wang, X. Teng, Y. Qin, et al., Ceram. Int. 47 (2021) 5739–5746.
[39] D. Wu, J. Song, Y. Ji, et al., J. Electroanal. Chem. 895 (2021) 115531.
[40] M. Liao, Q. Zhang, F. Tang, et al., Nanomaterials 8 (2018) 183.
[41] Z. Favors, W. Wang, H.H. Bay, et al., Sci. Rep. 4 (2015) 1–8.
[42] Y. Zhao, L. Zheng, H. Wu, et al., Electrochim. Acta 282 (2018) 609–617.
[43] W. Chang, C. Park, J. Kim, et al., Energ. Environ. Sci. 5 (2012) 6895–6899.
[44] Y. Zhang, X. Yuan, W. Lu, et al., Chem. Eng. J. 368 (2019) 525–532.
[45] Y. Cheng, Q. Li, C. Wang, et al., Small 13 (2017) 1–10.
[46] Z. Yi, Q. Han, P. Zan, et al., J. Mater. Chem. A 4 (2016) 12850–12857.
[47] M. Peng, Y. Qiu, M. Zhang, et al., Appl. Surf. Sci. 507 (2020) 145060.
[48] J. Ge, Q. Tang, H. Shen, et al., Ceram. Int. 46 (2020) 12507–12516.
[49] L. Yin, M. Wu, Y. Li, et al., New Carbon Mater. 32 (2017) 311–318.
[50] J. Bae, J. Son, J. Nanosci. Nanotechnol. 19 (2019) 1520–1524.
[51] S. Suh, H. Choi, K. Eom, et al., J. Alloy. Compd. 827 (2020) 154102.
[52] H. Huang, E. Kelder, L. Chen, et al., J. Power Sources 81 (1999) 362–367.
[53] P. Poizot, S. Laruelle, S. Grugeon, et al., Nature 407 (2000) 496–499.